Combined Bluntness and Roughness Effects on Cones at Hypersonic Speeds

Pedro Paredes,*
National Institute of Aerospace, Hampton, VA 23666, USA

Anton Scholten, †
North Carolina State University, Raleigh, NC 27695, USA

Meelan M. Choudhari,‡ Fei Li,§
NASA Langley Research Center, Hampton, VA 23681, USA

Bethany N. Price, ¶ Joseph S. Jewell,‖
Purdue University, West Lafayette, IN 47907, USA

This computational study investigates the effects of discrete roughness elements on a blunt cone at zero degrees angle of attack in a Mach 6 flow. Motivation was provided by experiments conducted in the Air Force Research Laboratory Mach 6 High Reynolds Number facility on a 7-degree half-angle cone with a roughness array located at 45 degrees from the apex on two nosetips of different blutness but equivalent roughness Reynolds number. Transition was only affected on the blunter cone, indicating that the transition onset is associated with the combined effects of bluntness and roughness. The present study investigates the 15.24 **mm nose radius,** 420 **azimuthal wavenumber case via Navier-Stokes computations of the laminar base flow and instability analysis. Plane-marching parabolized stability equations (PSE) and inflow-resolvent analysis based on the three-dimensional, harmonic linearized Navier-Stokes equations (HLNSE) are used to calculate the amplification of disturbances along the roughness wake as well as over the roughness nearfield. Results show that the roughness shape can have a great impact on the characteristics of the most amplified wake instabilities. For the experimental configuration with cubic roughness elements of** 15 μ**m height, the flow is marginally unstable. For prismatic elements of** 20 μ**m height, the PSE predicts a logarithmic disturbance amplification ratio of** $N = 5.6$ **along its wake, but this ratio increases to** $N = 9.6$ **when the amplification over the roughness and separation regions is included in the inflow-resolvent analysis.**

Nomenclature

E	=	total energy norm
f	=	disturbance frequency [s^{-1}]
G	=	energy gain
h_ξ	=	streamwise metric factor
h_ζ	=	azimuthal metric factor [m]
k	=	roughness height [m]
m	=	azimuthal wavenumber [rad^{-1}]
M	=	Mach number
N	=	Logarithmic amplification factor

*Research Engineer, Computational AeroSciences Branch, NASA LaRC. AIAA Senior Member
†Graduate Student, Department of Mechanical and Aerospace Engineering. AIAA Student Member
‡Research Scientist, Computational AeroSciences Branch. AIAA Fellow
§Research Scientist, Computational AeroSciences Branch.
¶Graduate Student, School of Aeronautics and Astronautics. AIAA Student Member
‖Assistant Professor, School of Aeronautics and Astronautics. AIAA Associate Fellow

$\hat{\mathbf{q}}$	=	vector of amplitude variables
$\breve{\mathbf{q}}$	=	vector of disturbance function variables
$\bar{\mathbf{q}}$	=	vector of base flow variables
$\tilde{\mathbf{q}}$	=	vector of perturbation variables
Re_{kk}	=	roughness Reynolds number
Re_k	=	roughness Reynolds number based on wall viscosity value
Re_∞	=	freestream unit Reynolds number [m^{-1}]
Re_{R_N}	=	Reynolds number based on nose radius
r_b	=	local radius of axisymmetric body at the axial station of interest [m]
R_N	=	nose radius [m]
T	=	temperature [K]
T_w	=	wall temperature [K]
$T_{w,ad}$	=	adiabatic wall temperature [K]
(u, v, w)	=	streamwise, wall-normal, and azimuthal velocity components [m s^{-1}]
(x, y, z)	=	Cartesian coordinates [m]
α	=	streamwise wavenumber [m^{-1}]
δ_h	=	boundary-layer thickness based on 99.5% total enthalpy [m]
Θ	=	boundary-layer momentum thickness [m]
κ	=	streamwise curvature [m^{-1}]
ω	=	disturbance angular frequency [s^{-1}]
ρ	=	density [kg m^{-3}]
(ξ, η, ζ)	=	streamwise, wall-normal, and azimuthal coordinates [m,m,rad]
θ	=	streamwise angle [°]
$\mathbf{M}$	=	energy weight matrix
Subscript		
∞	=	freestream value
0	=	inflow optimization location
1	=	outflow optimization location
R	=	reattachment location

I. Introduction

Laminar-turbulent transition of boundary-layer flows can have a strong impact on the performance of hypersonic vehicles because of its influence on the surface skin friction and aerodynamic heating. Therefore, the prediction and control of transition onset and the associated variation in aerothermodynamic parameters in high-speed flows are key issues for optimizing the performance of the next-generation aerospace vehicles. Although many practical aerospace vehicles have blunt, hemispherical and ogival nosetips, the mechanisms that lead to boundary-layer instability and transition on such geometries are often not well understood. A detailed review of boundary-layer transition over sharp and blunt cones in a hypersonic freestream is given by Schneider [1]. As described therein, both experimental and numerical studies have shown that the modal growth of Mack-mode instabilities (or, equivalently, the so-called second-mode waves) is responsible for laminar-turbulent transition on sharp, axisymmetric cones at zero degrees angle of attack. Studies have also shown that an increased nose-tip bluntness, i.e., a larger radius of hemispherical or ogival nosetips, leads to the formation of an entropy layer that may extend well beyond the vicinity of the nose-tip region [2]. The entropy layer has been shown to have a stabilizing effect on the amplification of Mack-mode instabilities, consistent with the experimental observation that the onset of transition is displaced downstream as the nose bluntness is increased. However, while the boundary-layer flow continues to become more stable with an increasing nose bluntness according to linear modal stability analysis, experiments indicate that the downstream movement in transition actually slows down and eventually reverses as the nose bluntness exceeds a certain critical threshold. The observed trend in transition onset at moderate to large values of nose bluntness is contrary to the predictions of linear stability theory, and therefore, it must be explained using a different paradigm. Even though no satisfactory theory has been proposed as yet to explain the phenomenon of transition reversal, the latter is believed to be somehow related to external forcing in the form of either surface roughness and/or freestream turbulence. Given the absence of modal instability as an underlying cause, nonmodal disturbance amplification induced by external forcing has been proposed as the basis of a physics-based model for the transition reversal phenomenon [3–6].

A collaborative effort was put forth under the NATO STO group AVT-240 on Hypersonic Boundary-Layer Transition Prediction focused on the problem of transition over axisymmetric cones with blunt hemispherical nosetips and on the potential role of transient growth in the transition reversal phenomenon [3, 5]. The comparison of wind tunnel measurements at freestream Mach numbers from 6 to 12 in both U.S. and European facilities showed two distinct regions referred to as "small bluntness" where the transition location moves downstream with increased bluntness and "large bluntness" where the transition location rapidly moves upstream. Furthermore, Stetson [2] identified an intermediate regime for "moderately-large bluntness" values, wherein transition still moves downstream as the nose bluntness is increased, but at a significantly slower rate. In these cases, the frustum transition is measured at locations where the Mack-mode waves are not sufficiently amplified, and yet the transition Reynolds number is lower than that for a sharp cone at the same flow conditions. Stetson [2] also observed that the measured transition locations within the transition-reversal regime were not easily reproducible across different runs. At a fixed set of freestream conditions, transition onset was found to vary across a wide range of frustum stations, and at times, the boundary layer flow remained laminar over the entire cone. Nonaxisymmetric transition patterns were observed even at zero degrees angle of attack, and the measured length of the transition zone was much larger than that for cones with smaller values of nose bluntness. Finally, Stetson [2] observed that frustum transition in the transition-reversal regime was highly sensitive to surface roughness in the nose-tip region. For smaller nose-tip bluntness prior to transition reversal, the surface finish on the nose tip (or the frustum) appeared to have no effect on frustum transition. Polishing the blunt nose tip before the wind tunnel run for the large bluntness cones resulted in either higher frustum transition Reynolds numbers or a completely laminar flow over the model. Primarily on the basis of this last observation, Stetson [2] speculated that frustum transition over large bluntness cones was dominated by disturbances originating near the nose tip. Therefore, roughness-induced transient growth appears to be a reasonable explanation for the transition-reversal phenomena in large bluntness cones at high speed. Subsequent work by Zanchetta [7] reported time-resolved heat transfer measurements on a 5-degree half-angle cone at at Mach 9. These measurements in the Imperial College Gun Tunnel revealed that the transition reversal regime was accompanied by transitional events that are initiated in the near-nose region and then convect downstream. The frequency of these events was linked to the severity of the roughness environment. The experimental investigation of roughness effects revealed that two-dimensional annular trips may be more effective at enhancing transition in the transition reversal regime than isolated three-dimensional roughness.

In summary, the available linear stability analyses [8–13] agree that the frustum transition for moderately large bluntness and the transition reversal at sufficiently large bluntness cannot be predicted solely based on modal instability amplification because Mack's second mode is strongly stabilized by the presence of the entropy layer, while the first mode, which is commonly responsible for the onset of transition at boundary-layer-edge supersonic conditions, is not destabilized. Additionally, the modal amplification of entropy-layer modes is marginal as reported by Refs. [5, 14, 15]. Because of the failure of the modal instability theory to predict the transition within the swallowing distance of the entropy layer, nonmodal growth was proposed by Paredes et al. [5] as the potential basis for a physics-based model for the experimentally observed onset of transition. Results indicate that stationary disturbances that are initiated within the nose-tip vicinity can undergo relatively significant nonmodal amplification that increases with the nose-tip bluntness. This finding does not provide a definite link between transient growth and the onset of transition, but is qualitatively consistent with the experimental observations [2, 5, 7] that frustum transition during the reversal regime was highly sensitive to wall roughness, and furthermore, was dominated by disturbances originating near the nose-tip. The predictions for optimal transient growth were used to design an azimuthally periodic array of microroughness elements located near the sonic point at the nose-tip [5]. Figure 1 shows that variable bluntness models with similar values of roughness Reynolds number, Re_{kk}, affected transition only on the blunter cone, demonstrating that transition onset in this case is associated with the combined effects of bluntness and roughness. The transient growth predictions of Paredes et al. [5] indicated that, for the same freestream unit Reynolds number, the maximum energy gain for short optimization intervals was about two times larger for the larger nose radius cone than for the smaller nose radius case. This finding is qualitatively consistent with the increased effectiveness of the roughness array on a blunter cone found in the experiments.

Finally, we note that wakes behind sufficiently large discrete-roughness elements can sustain large modal amplification of streak instabilities as shown by Choudhari et al. [16, 17], but the level of amplification is sensitive to the roughness parameters and other flow details [18]. Because the measured onset of transition during the AFRL experiments was within a short distance behind the roughness array, wake instability may have played a role in the large upstream shift in transition location. The present paper investigates that possibility via Navier-Stokes computations of the three-dimensional laminar boundary layer flow and multidimensional instability analysis. The methodology used to investigate the disturbance amplification is summarized in Section II. Then, the laminar boundary-layer flow over the

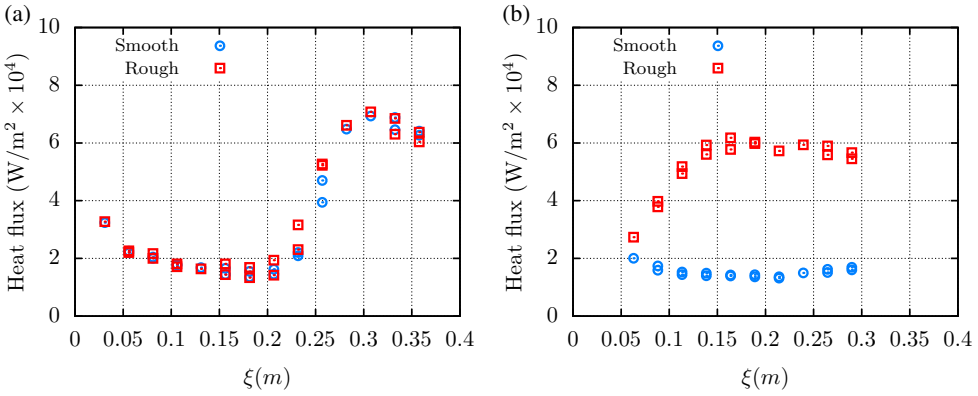

Fig. 1 Heat flux distributions for a 7° half-angle cone at $M_\infty = 5.9$ with a nose tip of (a) $R_N = 5.08$ mm rough ($Re_\infty = 66.5 \times 10^6$ m^{-1}, $k/\delta_h = 0.381$, $Re_{kk} = 294$) and smooth ($Re_\infty = 66.0 \times 10^6$ m^{-1}) and (b) $R_N = 15.25$ mm rough ($Re_\infty = 75.8 \times 10^6$ m^{-1}, $k/\delta_h = 0.225$, $Re_{kk} = 287$) and smooth ($Re_\infty = 76.9 \times 10^6$ m^{-1}) cone. The roughness consisted of equally spaced 15 μm cubical roughness elements (extracted from Ref. [5]).

selected configurations and instability results are presented in Section III. The summary and concluding remarks are presented in Section IV.

II. Theory

This section introduces the methodology behind the instability analysis described in this paper. The procedure closely follows the study of Paredes et al. [19] that analyzed the effects of wall-mounted vortex generators in Mack-mode waves and their streak instabilities in the boundary layer over a circular cone at flight conditions. Direct numerical simulations (DNS) are used to compute the three-dimensional, azimuthally-periodic, boundary-layer flow perturbed by the discrete roughness array. Similar to Ref. [19], the modal instability characteristics of the perturbed three-dimensional boundary-layer flow are studied by using the linear form of plane-marching PSE. Additionally, the current study uses the three-dimensional harmonic linearized Navier Stokes equations (HLNSE) to calculate the amplification of disturbances over the roughness elements and separation regions.

In what follows, freestream values are used as the reference values for nondimensionalization. The computational coordinates, (ξ, η, ζ), correspond to an orthogonal, body-fitted coordinate system, where ξ denotes the streamwise coordinate measured along the cone surface, η is the surface-normal coordinate, and ζ is measured along the azimuthal direction. The relevant metric factors are defined as

$$h_\xi = 1 + \kappa\eta, \tag{1}$$

$$h_\zeta = r_b + \eta\cos(\theta), \tag{2}$$

where κ denotes the streamwise curvature, r_b is the local radius, and θ is the local half-angle along the axisymmetric surface, i.e., $\sin(\theta) = \mathrm{d}r_b/\mathrm{d}\xi$.

The vector of perturbation variables is denoted by $\tilde{\mathbf{q}}(\xi, \eta, \zeta, t) = (\tilde{\rho}, \tilde{u}, \tilde{v}, \tilde{w}, \tilde{T})^T$ and the vector of disturbance functions is $\check{\mathbf{q}}(\xi, \zeta, \zeta) = (\check{\rho}, \check{u}, \check{v}, \check{w}, \check{T})^T$. The vector of basic state variables is $\bar{\mathbf{q}}(x, y, z) = (\bar{\rho}, \bar{u}, \bar{v}, \bar{w}, \bar{T})^T$. The linear perturbations are assumed to be harmonic in time and are written as

$$\tilde{\mathbf{q}}(\xi, \eta, \zeta, t) = \check{\mathbf{q}}(\xi, \eta, \zeta)\exp(-\mathrm{i}\omega t) + \text{c.c.}, \tag{3}$$

where the ω is the angular frequency, and c.c. refers to the complex conjugate.

The disturbance functions $\check{\mathbf{q}}(\xi, \eta, \zeta)$ satisfy the three-dimensional HLNSE [5], where the linear operators depend on the basic state variables and parameters, and on the angular frequency of the perturbation,

$$\mathbf{L}_{HLNSE}\check{\mathbf{q}}(\xi, \eta, \zeta) = \check{\mathbf{f}}, \tag{4}$$

where $\check{\mathbf{f}}$ represents an inflow condition or forcing term.

The PSE approximation to the HLNSE is applicable along the wake of the roughness because the basic state variables vary slowly along the streamwise direction. The PSEs are based on isolating the rapid phase variations in the streamwise direction via the disturbance ansatz

$$\breve{\mathbf{q}}(\xi,\eta,\zeta) = \hat{\mathbf{q}}(\xi,\eta,\zeta)\exp\left[\mathrm{i}\int_{\xi_0}^{\xi}\alpha(\xi')\,\mathrm{d}\xi'\right]. \tag{5}$$

The unknown streamwise varying wavenumber $\alpha(x)$ is determined in the course of the solution by imposing an additional constraint

$$\int_{\zeta}\int_{\eta}\hat{\mathbf{q}}^{*}\frac{\partial\hat{\mathbf{q}}}{\partial\xi}\,h_{\xi}\,h_{\zeta}\,\mathrm{d}\eta\,\mathrm{d}\zeta = 0. \tag{6}$$

Hence, the amplitude functions $\hat{\mathbf{q}}(\xi,\eta,\zeta) = (\hat{\rho},\hat{u},\hat{v},\hat{w},\hat{T})^{T}$ vary slowly in the streamwise direction in comparison with the phase term $\exp\left[\mathrm{i}\int_{\xi_0}^{\xi}\alpha(\xi')\,\mathrm{d}\xi'\right]$. Note that the amplitude function $\hat{\mathbf{q}}$ of Eq. (5) is three-dimensional because the present flow problem is inhomogeneous in the three spatial directions. Therefore, the conventional line-marching PSE that assumes homogeneous azimuthal direction of the basic state and amplitude functions is not applicable, and the plane-marching PSE are used instead. Substituting Eq. (5) into the HLNSE and invoking scale separation between the streamwise coordinate and the other two directions to neglect the viscous terms with streamwise derivatives, the plane-marching PSE are obtained in the form

$$\left(\mathbf{L}_{PSE} + \mathbf{M}_{PSE}\frac{1}{h_{\xi}}\frac{\partial}{\partial\xi}\right)\hat{\mathbf{q}}(\xi,\eta,\zeta) = 0, \tag{7}$$

where $\mathbf{L}_{PSE}$ indicate the linear operators of the plane-marching PSE and $\mathbf{M}_{PSE}$ has the terms multiplying the first-order streamwise derivatives in the linearized Navier-Stokes equations [20]. The initial disturbance profiles for the plane-marching PSE are obtained using a partial-differential-equation (PDE) based two-dimensional eigenvalue problem (EVP).

The onset of laminar-turbulent transition is estimated by using the logarithmic amplification ratio, the so-called N-factor, relative to the lower bound location ξ_I where the disturbance first becomes unstable,

$$N = -\int_{\xi_I}^{\xi}\alpha_i(\xi')\,\mathrm{d}\xi' + 1/2\ln\left[\hat{E}(\xi)/\hat{E}(\xi_I)\right]. \tag{8}$$

The energy norm of $\tilde{\mathbf{q}}$ was derived by Chu [21] and used by Mack [22] and Hanifi et al. [23] for linear stability theory is defined as

$$E(\xi) = \frac{1}{L_{\zeta}}\int_{\zeta}\int_{\eta}\tilde{\mathbf{q}}(\xi,\eta,\zeta)^{H}\mathbf{M}\tilde{\mathbf{q}}(\xi,\eta,\zeta)\,h_{\xi}\,h_{\zeta}\,\mathrm{d}\eta\,\mathrm{d}\zeta, \tag{9}$$

where h_{ξ} and h_{ζ} are the metric factors associated with the streamwise and azimuthal curvatures, respectively, the superscript H denotes the conjugate transpose, and $\mathbf{M}$ is the energy weight matrix equal to

$$\mathbf{M} = \mathrm{diag}\left[\frac{\bar{T}}{\gamma M^{2}\bar{\rho}},\bar{\rho},\bar{\rho},\bar{\rho},\frac{\bar{\rho}}{\gamma(\gamma-1)M^{2}\bar{T}}\right]. \tag{10}$$

Traditionally, the instability of roughness elements has been studied by analyzing the wake of the roughness elements with two-dimensional, quasiparallel eigenvalue analysis [e.g., 17, 18, 24–27] or plane-marching PSE [e.g., 28–31]. The plane-marching PSE calculation of the roughness wake instabilities are initiated just downstream of the reattachment location in the present paper.

Additionally, the amplification of disturbances over the vicinity of the roughness elements, where flow separation is present and the streamwise gradients of the base flow variables are comparable to azimuthal and wall-normal gradients, is studied by using the fully three-dimensional HLNSE method. Due to the absence of unstable instabilities upstream of the roughness elements in the present strong pressure gradient flow, the inflow-driven optimal growth or inflow-resolvent analysis, previously used for two-dimensional or axisymmetric configurations [e.g., 5, 32], is used for the current three-dimensional problem by solving the full three-dimensional direct and adjoint HLNSE. The optimal initial disturbance, $\tilde{\mathbf{q}}_0$, is defined as the initial (i.e., inflow) condition at ξ_0 that maximizes the objective function, J, which is defined as a measure of disturbance growth over a specified interval $[\xi_0,\xi_1]$. The definition used in the present study corresponds to the outlet energy gain $J = G^{out}$ that is defined as

$$G^{out} = \frac{E(\xi_1)}{E(\xi_0)}. \tag{11}$$

The variational formulation of the problem to determine the maximum of the objective functional J leads to an optimality system [33], which is solved in an iterative manner, starting from a random solution at ξ_0 that must satisfy the boundary conditions. The HLNSE, RHLNSE, or PSE, $\mathbf{L}\tilde{\mathbf{q}} = 0$, are used to integrate $\tilde{\mathbf{q}}$ up to ξ_1, where the final optimality condition is used to obtain the initial condition for the backward adjoint equations integration, $\mathbf{L}^\dagger\tilde{\mathbf{q}}^\dagger = 0$. At ξ_0, the adjoint solution is used to calculate the new initial condition for the forward integration with the initial optimality condition. The iterative procedure finishes when the value of G has converged up to a certain tolerance, which was set to 10^{-4} in the present computations.

The plane-marching PSE are discretized with high-order finite-difference schemes [34, 35] of sixth order for the crossplane of wall-normal and azimuthal coordinates with $N_\eta = 101$ and $N_\zeta = 61$ points, respectively. The PSE are integrated along the streamwise coordinate by using second-order backward differentiation and with enough grid points to ensure convergence of the results. The HLNSE are discretized with twelfth-order finite-difference schemes along the wall-normal and azimuthal coordinates with $N_\eta = 51$ and $N_\zeta = 31$, respectively. The streamwise coordinate is discretized with a fourth-order centered finite-difference scheme with $N_\xi = 701$ points for a streamwise domain of $\xi \in [11.8, 13.8]$ mm. Because of the selected discretization scheme along x, the matrix $\mathbf{L}_{HLNSE}$ of Eq. (4) becomes a block pentadiagonal matrix. The linear system is solved by using a combined multithread and multiprocessor algorithm based on the Thomas algorithm and the dual Schur complement method [36]. The inflow plane at $\xi_0 = 11.8$ mm is used as the inflow optimization location and an interior plane of this solution at $\xi_1 = 12.6$ mm is used as the outflow optimization location to exclude any effects of the outflow boundary condition on the HLNSE solution.

The plane-marching PSE and HLNSE use the same wall-normal and azimuthal boundary conditions. No-slip, isothermal boundary conditions are used at the wall, i.e., $\hat{u} = \hat{v} = \hat{w} = \hat{T} = 0$. The amplitude functions are forced to decay at the farfield boundary by imposing the Dirichlet conditions $\hat{\rho} = \hat{u} = \hat{w} = \hat{T} = 0$. The farfield boundary coordinate is set just below the shock layer. Only one half of the roughness wavelength $\lambda_{ST} = 2\pi/m_{ST}$, where m_{ST} denotes the streak wavenumber, needs to be discretized and the boundary conditions at $\zeta = -\lambda_{ST}/2$ and $\zeta = 0$, either symmetric (S), i.e., $(\hat{\rho}_z, \hat{u}_z, \hat{v}_z, \hat{w}\ , \hat{T}_z)^T = \mathbf{0}$, or antisymmetric (A), i.e., $(\hat{\rho}\ , \hat{u}\ , \hat{v}\ , \hat{w}_z, \hat{T}\ )^T = \mathbf{0}$, determine the nature of the instability mode, i.e., whether the disturbance is sinuous or antisymmetric (AA and SA) or varicose or symmetric (SS and AS) type. Note that fundamental disturbances (AA and SS types) correspond to $m = m_{ST}$, whereas subharmonic disturbances (SA and AS types) analyzed herein correspond to $m = 1/2\, m_{ST}$. The azimuthal boundary conditions used in each case are explained in Paredes et al. [37].

The number of discretization points in all three directions and the wall-normal domain size were varied to ensure that the relevant flow quantities were insensitive to further improvement in grid resolution and enlargement of the domain size.

III. Results

This section presents the computational investigation of the experimental data pertaining to the effects of discrete roughness elements located on the nosetip of variable bluntness, 7-degree cones. The freestream conditions match those from the experiments by Ref. [5] shown in figure 1 in the Air Force Research Laboratory (AFRL) Mach 6 High Reynolds Number facility.

A. Laminar Boundary-Layer Flows

The basic state used in the present analysis corresponds to the laminar boundary-layer flow over the array of roughness elements on the 7-degree half-angle blunt cone with a nose radius of 15.24 mm.

1. Unperturbed Boundary-Layer Flow

The unperturbed, laminar boundary-layer flow over the cone surface is computed by using a second-order accurate algorithm as implemented in the finite-volume compressible Navier-Stokes flow solver VULCAN-CFD* [38]. The VULCAN-CFD solution is based on the full Navier-Stokes equations and uses the solver's built-in capability to iteratively adapt the computational grid to the shock. Sutherland's law for air is used to calculate the dynamic viscosity as a function of temperature.

The AFRL Mach 6 facility operates at stagnation pressures p_0 from 700 to 2100 psi (4.83 to 14.5 MPa). The working fluid is air and is treated as an ideal gas because of the relatively low temperature and pressure. The blunt cones used in the experiments by Stetson [2] had a half-angle of 8° and a base radius of 2.0 in. (0.0508 m). A total of

*visit `http://vulcan-cfd.larc.nasa.gov` for further information about the VULCAN-CFD solver

196 experiments encompassing 108 unique conditions comprised the Stetson [2] Mach 6 results. The present analysis considers the 7° half-angle variable-bluntness cone that was used in the experiments in the AFRL Mach 6 facility by Jewell et al. [13]. The configuration selected for the present study is specified in Table 1 and corresponds to the $R_N = 15.24$ mm cone used in the roughness experiments of [5].

Table 1 Details of the configuration used in the present study.

R_N [mm]	Re_∞ [$\times 10^6$ m^{-1}]	M_∞	T_∞ [K]	T_w [K]	$T_w/T_{w,ad}$	ρ_∞ [kg $\cdot$ m^{-3}]	p_0 [psi]
15.24	75.8	5.9	76.74	300	0.57	0.335847	1526.23

2. Perturbed Boundary-Layer Flow

The axisymmetric boundary-layer flow is perturbed via arrays of axially localized roughness elements centered at selected axial stations. The roughness array is comprised of cube- or prism-shaped elements. The three-dimensional, azimuthally-periodic, laminar boundary-layer flow over the cone surface with arrays of wall-mounted roughness elements is computed by using a high-order DNS solver that was recently used by Li et al. [39] to simulate the excitation of stationary crossflow vortices behind an array of roughness elements mounted on a yawed cone. A detailed description of the governing equations and their numerical solution is given by Wu and Martin [40]. The inviscid fluxes from the governing equations are computed using a seventh-order weighted essentially nonoscillatory finite-difference WENO scheme introduced by Jiang and Shu [41]; the present scheme also allows the use of limiters that have been optimized to reduce the numerical dissipation. Both an absolute limiter on the WENO smoothness measurement and a relative limiter on the total variation are employed simultaneously during the simulation. The viscous fluxes are discretized using a fourth-order central difference scheme and time integration is performed using a third-order low-storage Runge-Kutta scheme [42].

The geometry of the roughness elements used in the present computations is selected, in part, on the basis of the earlier experiments reported in Ref. [5]. Specifically, the conditions of Table 1 were used to study the effect on transition location of an array of 15 μm height laser-machined roughness elements with an approximately cubical shape located at 45° from the apex of the spherical tip, which is near the sonic line for zero degrees angle of attack. The number of roughness elements was selected to match the optimal disturbance azimuthal wave number that leads to maximum transient growth at the same conditions. Specifically, 210 roughness elements were mounted on the small radius cone ($R_N = 5.08$ m), and 420 roughness elements were mounted on the larger radius cone ($R_N = 15.24$ mm). The present investigation considers the 15 and 20 μm tall cubic elements, as well as prismatic roughness elements with the same heights but with a larger width and length equal to 50% of the corresponding azimuthal wavelength. The roughness arrays are located at 45° from the apex of the spherical tip of the $R_N = 15.24$ μm cone with an azimuthal wavenumber of $m_{ST} = 420$. Table 2 shows the boundary-layer edge properties at the location of the roughness elements, $\theta = \xi/R_N = 45$ deg, and Table 3 shows the roughness variables for the investigated configurations. The value of Re_{kk} is slightly different to the value reported by Paredes et al. [5] due to the used Sutherland's viscosity law for the present calculations. The roughness parameters corresponding to both 15 and 20 μm roughness heights are supercritical based on both the ballistics-range data [43–45] and a transient growth correlation [46, 47].

Table 2 Boundary-layer properties at the location of the roughness elements, $\theta = \xi/R_N = 45$ deg.

δ_h [μm]	Θ [μm]	M_e	T_e [K]	u_e [m/s]	ρ_e [kg/m^3]
72.175	7.4676	1.098	491.8	488.0	1.284

Figures 2(a)-2(d) display three-dimensional views of three azimuthal wavelengths of the roughness array over the cone with $R_N = 15.24$ mm and a roughness array located at $\theta = 45°$ from the apex of the spherical tip of (a) 15 μm and (b) 20 μm cubic elements, and (c) 15 μm and (d) 20 μm prismatic elements with height and width and length equal to half the wavelength of the array (so they represent a 50% azimuthal blockage). The surface of the cone and roughness elements are shown in gray. The separation regions are shown as a black isosurface. Isolines of Mach number values at selected streamwise stations are also shown. The disturbances induced by the roughness elements evolve into streamwise elongated streaks. Figures 2(a) and 2(b) show that azimuthal variations across the wakes of the 15 μm and 20 μm cubic roughness elements decay within a short streamwise distance in comparison with the nosetip

Table 3 Properties of the roughness elements used in the present study. The roughness elements are located at $\theta = 45°$. The local Reynolds number based on momentum thickness is defined as $Re_\Theta = \rho_e u_e \Theta/\mu_e$. The roughness Reynolds numbers are defined as $Re_k = \rho(k)u(k)k/\mu_w$ and $Re_{kk} = \rho(k)u(k)k/\mu(k)$. The roughness Reynolds number critical value for nosetip transition onset from ballistics-range experiments [45] is $Re_{k,c} = 250$. Additionally, the critical value for the revised PANT correlation [44] is $Re_\theta((k/\Theta)(T_e/T_w))^{1.3} = 574$ and for the transient growth based correlation [46] is given by $Re_\theta(k/\Theta)(T_e/T_w)^{1.27} = 434$.

k [μm]	k/δ_h	k/Θ	Re_k	Re_{kk}	$Re_\Theta((k/\Theta)(T_e/T_w))^{1.3}$	$Re_\Theta(k/\Theta)(T_e/T_w)^{1.27}$
15	0.208	2.01	415	337	834	667
20	0.277	2.68	616	482	1,213	889

radius. Furthermore, the wakes of the cubic elements do not spread across the entire azimuthal wavelength, which indicates that they are equivalent to the wakes of discrete roughness elements. The short extent of the roughness wake was also observed by Theiss et al. [24], who analyzed the wake flow instabilities behind discrete roughness elements on a generic spherical reentry capsule. However, the roughness array with prismatic elements of 50% azimuthal blockage shows a modulation of the boundary layer over the entire azimuthal wavelength and a much longer streamwise extent of azimuthal variations in the array wake.

B. Instability Analysis

The instability characteristics of the perturbed, streaky boundary-layer flows are examined next. The plane-marching PSE are used to monitor the evolution of the streak instabilities that become amplified along the wake of the roughness elements and can dominate the process of laminar-turbulent transition. Because a stable and robust integration of the plane-marching PSE can only be initiated downstream of the separation region that forms behind the the roughness elements, the three-dimensional HLNSE are also used to help capture the disturbance evolution in the immediate vicinity of the roughness element with 20 μm height and 50% azimuthal blockage configuration that corresponds to the most unstable case.

Figures 3(a)-3(d) show the N-factor curves for symmetric and antisymmetric instability modes with azimuthal wavelengths that correspond to the fundamental wavelength of the roughness element and its first subharmonic for the various configurations shown in Figs. 2(a)-2(d), respectively. For the cubic elements, the fundamental (AA and SS) and subharmonic (SA and AS) instability modes are equally amplified because the wake behavior is similar to that behind isolated roughness elements. For the 15 μm cubic roughness elements, Fig. 3(a) shows that the antisymmetric modes (AA and SA) are marginally amplified with a maximum N-factor equal to $N \approx 0.16$ for $f = 2.0$ MHz at $\theta = 45.8°$, and the symmetric modes (SS and AS) are even less amplified. When the height of the cubic roughness elements is increased from 15 μm to 20 μm, Fig. 3(b) shows that the symmetric modes become dominant, with a maximum N-factor of $N \approx 3$ for $f = 6.0$ MHz at $\theta = 46.7°$, while the antisymmetric modes reach approximately $N = 1.9$ for $f = 5$ MHz at $\theta = 47.4°$. However, the roughness elements of the same height (15 μm) as the marginally unstable case from Fig. 3(a) but a larger planform size (Fig. 3(c)), the PSE predict a maximum N-factor of $N = 1.9$ at $\theta = 48.2°$, which is attained by a subharmonic antisymmetric (SA) mode with $f = 1.0$ MHz that is slightly more amplified than the fundamental antisymmetric (AA) mode. The symmetric modes with fundamental (SS) and subharmonic (AS) azimuthal wavelengths reach a peak of $N = 1.4$ for $f = 2.5$ MHz in this case. Similar to the comparison of the N-factors for the 15 μm height cubic (Fig. 2(a)) and prismatic (Fig. 2(c)) roughness elements, the maximum N-factor values for the prismatic roughness elements with 20 μm height (Fig. 2(d)) are higher than those for the 15 μm cubic elements (Fig. 2(b)). Wake instabilities behind the prismatic elements attain a maximum N-factor of $N = 5.6$ for the symmetric SS and AS modes at 47.7° and a lower maximum $N = 4.3$ for the subharmonic, antisymmetric SA mode and slightly lower for the fundamental antisymmetric AA mode at the same location of 49.4°. One may also observe that most of the N-factor curves from Figs. 3(a)-3(d) show a nonzero slope at the initial marching station that is located just downstream of the reattachment location θ_R behind the roughness element. The plane-marching PSE require the basic state variables to have a slow spatial variation along the streamwise direction; however, this requirement is unlikely to be met within the short recirculation region induced by the roughness elements.

For the case of prismatic roughness elements with 20 μm height and 50% azimuthal blockage, we also used an inflow resolvent or optimal growth analysis based on the three-dimensional HLNSE in order to study the evolution of linear disturbances over the entire flow field, including the near field of the roughness elements. In this case,

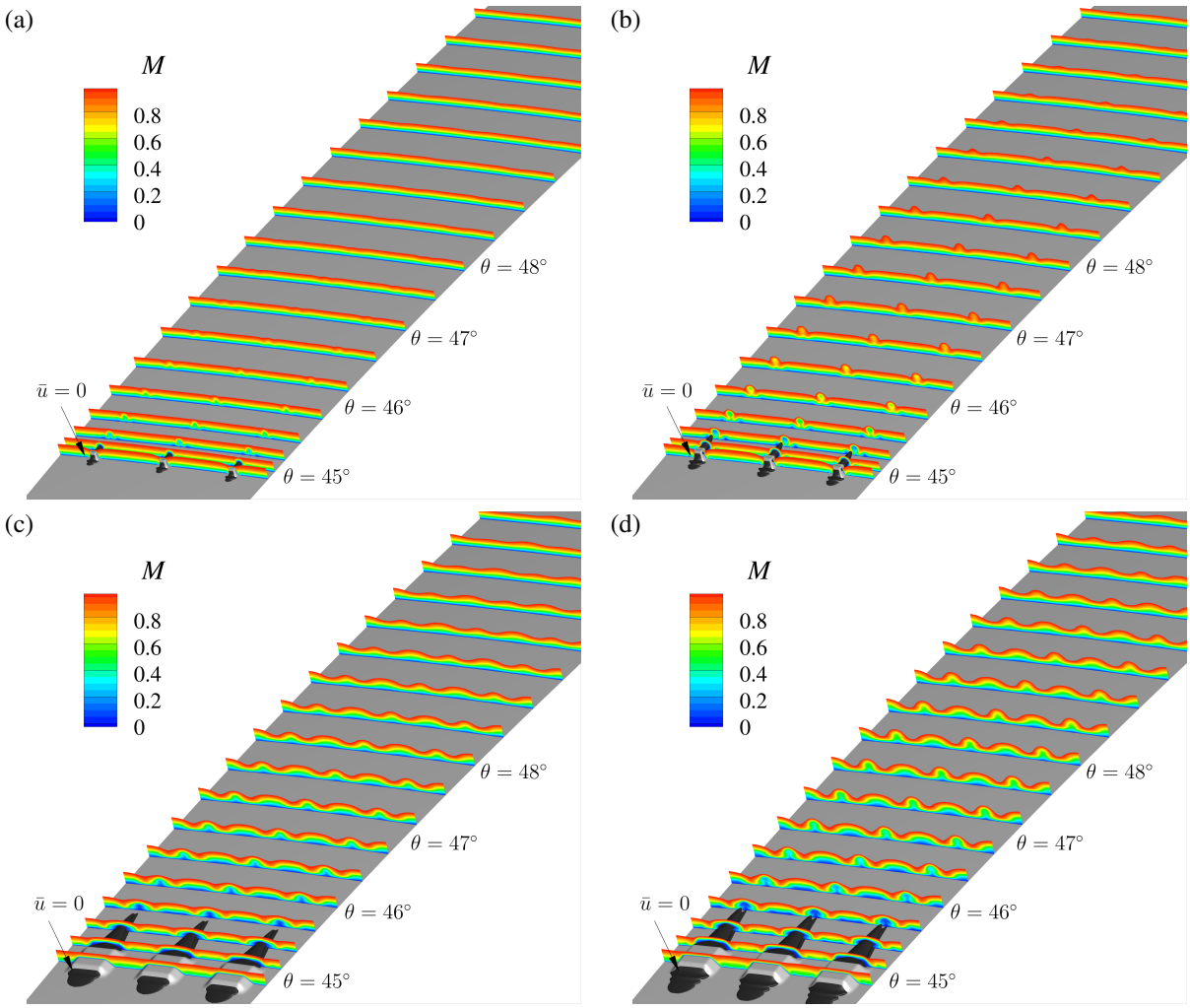

Fig. 2 Three-dimensional view of three azimuthal wavelengths of the modulated hypersonic boundary-layer flows corresponding to the $R_N = 15.24$ mm cone with an array of 420 roughness elements located at 45° from the apex of the spherical tip. The roughness elements correspond to either cubic shapes with a height equal to (a) 15 μm and (b) 20 μm, or prismatic shapes with (c) 15 μm and (d) 20 μm height and 50% azimuthal blockage with respect to the azimuthal spacing between the centers of each pair of adjacent roughness elements. The wall is shown in gray whereas regions of recirculating flow are shaded in black. Isolines of Mach number values are shown in wall-normal planes at selected streamwise locations.

the ratio of the distance from the roughness to the reattachment location to the distance from the roughness to the maximum N-factor location is equal to 0.27, and the largest growth rates actually occur at the reattachment location as seen from Fig. 3(d). Therefore, the previously described analysis based on the plane-marching PSE starting from the reattachment location is likely to exclude a significant portion of the instability amplification. Due to the absence of unstable disturbances upstream of the roughness element, we elect to compute the optimal inflow disturbance just upstream of the roughness elements at $\theta_0 = \xi_0/R_N = 44.36$ deg. Based on the results in Fig. 3(d) that were based on the plane-marching PSE, the final optimization location is selected at $\theta_1 = \xi_1/R_N = 47.4°$ in order to allow for the streak instability modes to develop. The resulting N-factor curves for the symmetric and antisymmetric instability modes at the fundamental and subharmonic azimuthal wavelengths are presented in Figure 4. Regardless of the type of instability mode or the value of disturbance frequency, the N-factor curves based on the inflow resolvent begin with a short region of rapid initial amplification that is attributed to transient growth from the inflow location up to the leading edge of the roughness element. The disturbances experience a slight decay at the roughness leading edge, and begin to grow again downstream of the trailing edge of the roughness elements. The location where the disturbances resume their

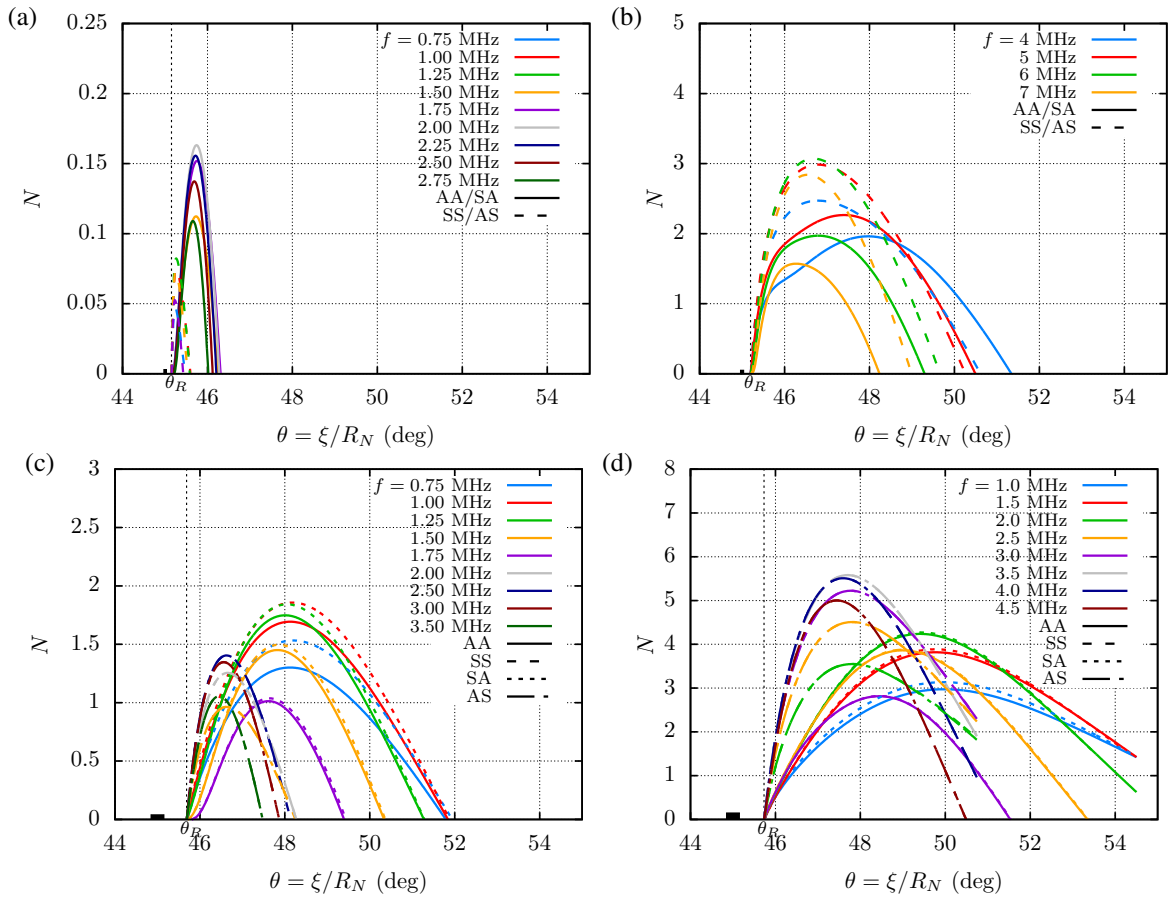

Fig. 3 *N*-**factor curves calculated with plane-marching PSE for streak instability modes of the modulated hypersonic boundary-layer flows corresponding to the** $R_N = 15.24$ **mm cone with (a)** 15 μ**m and (b)** 20 μ**m height cubic elements, and (c)** 15 μ**m and (d)** 20 μ**m height and** 50% **azimuthal blockage prismatic elements. The most amplified disturbance frequencies are selected for each case. The roughness elements and corresponding reattachment locations are indicated with a black rectangle and a dashed black vertical line at** θ_R**, respectively.**

amplification downstream of the roughness elements increases with an increasing value of the frequency parameter. Also, the symmetric disturbances (AS and SS) experience both earlier and stronger onset of amplification over the separated region in comparison with the antisymmetric disturbances (AA and SA). The most amplified disturbances correspond to the symmetric SS and AS modes, which are nearly equally amplified, with a frequency of 2.5 MHz that reach $N = 9.6$. In comparison with the maximum N-factor of 5.6 based on the PSE (which is attained by a symmetric disturbance with $f = 3.5$ MHz as shown in Fig. 3(d)), the HLNSE-based N-factor value is 71% higher and the predicted value of the most amplified disturbance frequency has reduced by 29%, from 3.5 MHz to 2.5 MHz. The most amplified antisymmetric disturbance reaches $N = 6.8$ and corresponds to the subharmonic antisymmetric SA mode with a frequency of 1.5 MHz.

To quantify the differences between the plane-marching PSE and the 3D, inflow-resolvent based HLNSE predictions, the N-factor curves of the most amplified disturbances are shown in Fig. 5(a). Results show that an upward shift by $\Delta N = 5.1$ in the PSE based N-factor curve for the AS mode with $f = 2.5$ MHz leads to a nearly perfect overlap with the HLNSE based N-factor curve. A similar collapse occurs when $\Delta N = 2.9$ is added to the PSE predictions for the SA mode with $f = 1.5$ MHz. Therefore, the optimal growth disturbance predicted by the inflow-resolvent analysis reduces to the modal streak instabilities downstream of the roughness element. The HLNSE are able to account for the disturbance amplification over the roughness element and the separation region. Previous DNS [31] had shown that the extent of disturbance growth within the nearfield of the roughness elements increases with an increasing streamwise extent of a sinusoidal roughness patch for a supersonic zero-pressure-gradient flat-plate boundary layer. However, in that

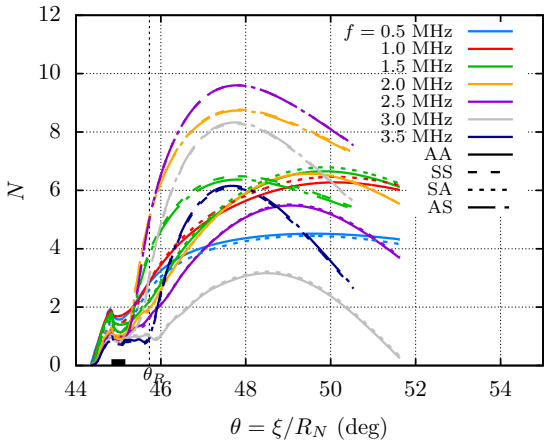

Fig. 4 ***N*-factor curves calculated with three-dimensional HLNSE for streak instability modes of the modulated hypersonic boundary-layer flows corresponding to the R_N = 15.24 mm cone with 20 μm height and 50% azimuthal blockage prismatic elements. The roughness element and corresponding reattachment location are indicated with a black rectangle and a dashed black vertical line at θ_R, respectively.**

work, the difference between the peak N-factor based on wake amplification predicted with PSE and the total disturbance growth including the nearfield region of a localized roughness element array was rather modest. On the other hand, the near field disturbance growth is larger than even the total amplification downstream of the reattachment location, a characteristic that may be associated with the placement of the roughness array within a strong favorable pressure gradient region. Even if one discounts the initial transient growth as potentially unrealizable in a real disturbance environment, the corresponding difference becomes $\Delta N \approx 4.3$ in the present case. The N-factor spectra calculated with the PSE and HLNSE methods at $\theta = 48°$ are compared in Fig. 5(b). The shifts in N-factor values and the frequency bands for the symmetric and antisymmetric modes between the PSE and HLNSE predictions are rather significant and underscore the importance of accounting for the disturbance amplification within the region of separated flow.

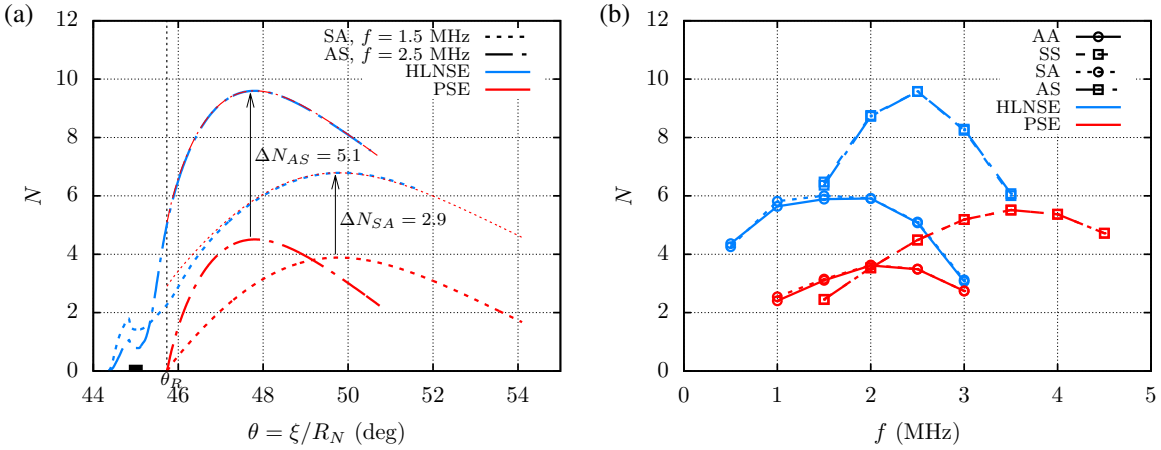

Fig. 5 (a) Comparison of *N*-factor curves and (b) spectra at θ = 48° calculated with three-dimensional HLNSE and plane-marching PSE for streak instability modes of the modulated hypersonic boundary-layer flows corresponding to the R_N = 15.24 mm cone with 20 μm height and 50% azimuthal blockage prismatic elements. The roughness element and corresponding reattachment location are indicated with a black rectangle and a dashed black vertical line at θ_R, respectively.

Next, we examine the spatial structure of the most amplified modes of both antisymmetric and symmetric types, as determined from the inflow resolvent based on the 3D HLNSE. Figure 6 shows a three-dimensional view of a pair of isosurfaces corresponding to $\tilde{u} = \pm 5$, respectively, for the SA mode with f = 1.5 MHz and the AS mode with

f = 2.5 MHz. Here, $\tilde{u}$ denotes the normalized velocity perturbation such that the inflow disturbance has an energy norm (Eq. 9) of $E_0 = 1$. In the strong shear layer over the separated zone near the roughness elements, the symmetric disturbances grow more strongly than the antisymmetric mode. Consequently, for the same level of streamwise velocity perturbation ($|\tilde{u}| = 5$), the isosurfaces for the symmetric mode begin significantly farther upstream than the isosurfaces for the antisymmetric mode. As shown in the N-factor curves (Fig. 4), the amplification of the symmetric disturbances terminates earlier within the wake region, with the peak N-factors near $\theta = 47.8°$. The isosurfaces of Fig. 6(b) begin to shrink downstream of that location. On the other hand, the maximum amplitude of the antisymmetric disturbance is attained farther downstream at $\theta \approx 50°$, and hence, the isosurfaces for the antisymmetric disturbance continue to expand throughout the axial length of the plotted domain.

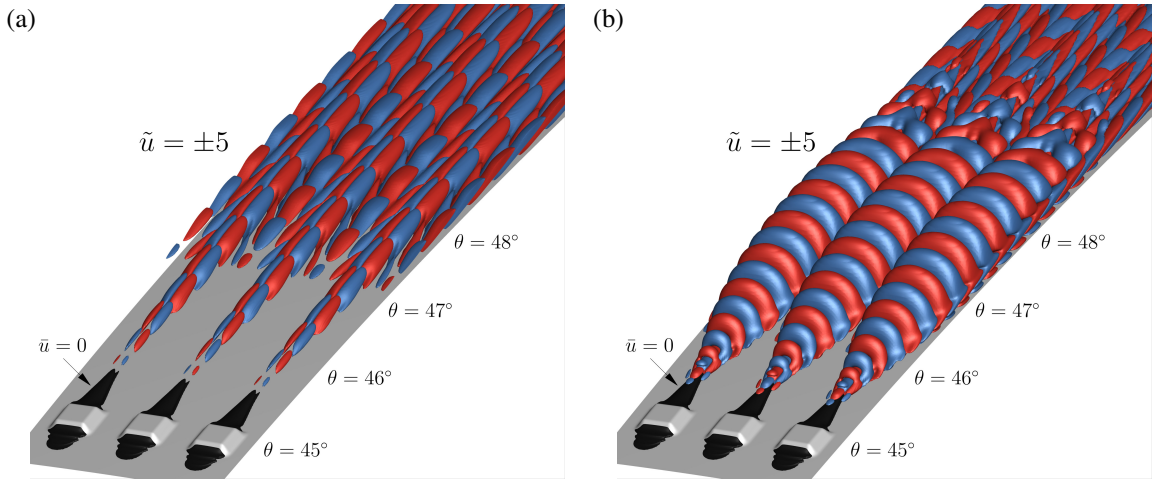

Fig. 6 Isosurfaces of streamwise velocity perturbation $\tilde{u} = \pm 5$ normalized with the inflow energy at $\theta_0 = 44.36°$ and calculated with three-dimensional HLNSE for the most amplified antisymmetric and symmetric streak instability modes, i.e., (a) SA with $f = 1.5$ MHz and (b) AS with $f = 2.5$ MHz, respectively, of the modulated hypersonic boundary-layer flows corresponding to the $R_N = 15.24$ mm cone with 20 μm height and 50% azimuthal blockage prismatic elements. The separated flow regions, $\bar{u} = 0$ are shown as black isosurfaces.

IV. Summary and Concluding Remarks

The present computational study investigated the combined effect of bluntness and discrete roughness elements within the nosetip region of a 7-degree half-angle cone at zero degrees angle of attack. The nose radius and freestream conditions were chosen to match a subset of the experiments in the AFRL Mach 6 High Reynolds Number facility that investigated roughness effects on transition over a cone model with replaceable nose-tips of 5.08 mm and 15.24 mm radii. The experiments used a laser-machined, azimuthally-periodic array of 15 μm tall cubic roughness elements located at 45 degrees from the apex of the spherical tip, which nearly coincided with the sonic location. The roughness array spacing was designed to match the optimal wavenumber for maximum transient growth, namely, $m = 210$ for a nose radius of 5.08 mm and $m = 420$ for the blunter cone tip with 15.24 mm nose radius. With a similar $Re_{kk} = 300$ for both sets of nosetip and roughness array parameters, the measurements in the AFRL facility showed that the roughness elements had an effect on the transition location only for the blunter cone. An implication of this finding was that the measured onset of transition might have been associated with the combined effects of nosetip bluntness and the roughness elements [5].

Herein, a computational investigation was conducted using the blunter nosetip configuration from the experiment and a matching set of freestream conditions. However, in addition to investigating the potential role of the cubic roughness elements from the experiments, other roughness shapes and heights were also included in the present study. Navier-Stokes computations of the roughness-induced distortion of the laminar boundary layer and multidimensional disturbance analysis of the distorted flow utilizing the plane-marching parabolized stability equations (PSE) and an inflow driven resolvent analysis based on the three-dimensional, harmonic linearized Navier-Stokes equations (HLNSE), were used to investigate the disturbance amplification characteristics within a boundary layer perturbed by different arrays of roughness elements.

The PSE computations of the wake instability for roughness arrays located at 45 degrees from the apex of the

spherical nose tip showed that the roughness wake should have sustained a modal instability at the experimental conditions; however, the predicted maximum amplification ratio behind that array was rather small, i.e., corresponding to a peak N-factor of just 0.16. Furthermore, the prismatic roughness elements with the same height of 15 μm, but length and width corresponding to a 50% azimuthal blockage led to stronger streak instabilities that reached a peak N-factor of 1.9. By increasing the roughness height to 20 μm, the wake instabilities reached a maximum N-factor of nearly 3 for the cubic roughness elements and a still modest value of 5.6 for the prismatic elements with higher blockage. However, the integration of the plane-marching PSE began at a finite distance behind the roughness array, set at the end of the recirculating region downstream the roughness array. Computations indicated a nonzero growth rate of the most amplified wake instabilities at this initial location, suggesting that the plane-marching PSE would not account for a portion of the disturbance growth near the roughness elements/ A similar finding was demonstrated in our previous work involving DNS and HLNSE computations for a roughness patch in a supersonic boundary layer [48].

To account for the total amplification of disturbances over the entire flow field, an inflow resolvent or optimal growth analysis based on the three-dimensional HLNSE was used for the most unstable case of the 20 μm prismatic roughness elements. As expected, the N-factor curves from the PSE and optimal growth HLNSE were found to become parallel within the wake of the roughness element, with the primary difference being the extra amplification captured by the HLNSE in the vicinity of the roughness element, including the regions of flow separation. The HLNSE analysis predicted a maximum N-factor of 9.6, which represents an increase of nearly 71% with respect to the PSE prediction. The most amplified disturbance was predicted to be a symmetric or varicose instability with a frequency of 1.5 MHz, while the PSE predicted a most amplified disturbance frequency of 2.5 MHz.

Despite the extra amplification captured by including the nearfield of the cubic roughness elements, the peak N-factor for the 15 μm height elements from the experiment remains rather small, and hence, is unlikely to explain the observed onset of transition behind these elements. However, a possible underestimation of the roughness height, planform size, and/or step, could raise the currently low N-factor just enough to reach the low threshold for transition in a conventional facility. Thus, further experiments and numerical investigations are required to explain the measured transition in the AFRL experiment as well as the onset of transition behind nosetip roughness elements on blunt cone configurations. Future testing will be conducted at Purdue's Boeing/AFOSR Mach 6 Quiet Tunnel (BAM6QT) in both quiet, low-noise conditions and conventional noisy conditions for similar nosetip Reynolds numbers. IR thermography and pressure sensors will be used to identify transition location and visualize the wake downstream of the trips, while high-speed schlieren visualization will be used to image the boundary layer and identify structures within it.

Acknowledgments

This material is based upon research supported in part by the U. S. Office of Naval Research under award number N00014-20-1-2261 monitored by Dr. Eric Marineau and in part by the Hypersonic Technology Project (HTP) under the Aeronautics Research Mission Directorate (ARMD). The computational resources supporting this work were provided by the DoD High Performance Computing Modernization Program, the NASA High-End Computing (HEC) Program through the NASA Advanced Supercomputing (NAS) Division at Ames Research Center and the LaRC K-Midrange Cluster at Langley Research Center.

References

[1] Schneider, S., "Hypersonic Laminar-Turbulent Transition on Circular Cones and Scramjet Forebodies," *Progress in Aerospace Sciences*, Vol. 40, 2004, pp. 1–50. doi:10.1016/j.paerosci.2003.11.001.

[2] Stetson, K., "Nosetip Bluntness Effects on Cone Frustum Boundary Layer Transition in Hypersonic Flow," AIAA Paper 83-1763, 1983. doi:10.2514/6.1983-1763.

[3] Paredes, P., Choudhari, M., Li, F., Jewell, J., Kimmel, R., Marineau, E., and Grossir, G., "Nosetip Bluntness Effects on Transition at Hypersonic Speeds: Experimental and Numerical Analysis Under NATO STO AVT-240," AIAA Paper 2018-0057, 2018. doi:10.2514/6.2018-0057.

[4] Cook, D., Thome, J., Brock, J., Nichols, J., and Candler, G., "Understanding Effects of Nose-Cone Bluntness on Hypersonic Boundary Layer Transition using Input-Output Analysis," AIAA Paper 2018-0378, 2018. doi:10.2514/6.2018-0378.

[5] Paredes, P., Choudhari, M., Li, F., Jewell, J., Kimmel, R., Marineau, E., and Grossir, G., "Nosetip Bluntness Effects on Transition at Hypersonic Speeds," *Journal of Spacecraft Rockets*, Vol. 56, No. 2, 2019, pp. 369–387. doi:10.2514/1.A34277.

[6] Paredes, P., Choudhari, M., Li, F., Jewell, J., and Kimmel, R., "Nonmodal Growth of Traveling Waves on Blunt Cones at Hypersonic Speeds," AIAA Paper 2019-0876, 2019. doi:10.2514/6.2019-0876.

[7] Zanchetta, M., "Kinetic Heating and Transition Studies and Hypersonic Speeds," Ph.D. thesis, Imperial College of Science, Technology and Medicine, London, 1996. URL https://spiral.imperial.ac.uk/handle/10044/1/37124.

[8] Malik, M., Spall, R., and Chang, C.-L., "Effect of Nose Bluntness on Boundary Layer Stability and Transition," AIAA Paper 90-0112, 1990. doi:10.2514/6.1990-112.

[9] Herbert, T., and Esfahanian, V., "Stability of Hypersonic Flow over a Blunt Body," AGARD CP-514. Paper 28. Theoretical and Experimental Methods in Hypersonic Flows, 1994.

[10] Marineau, E., Moraru, C., Lewis, D., Norris, J., Lafferty, J., Wagnild, R., and Smith, J., "Mach 10 Boundary-Layer Transition Experiments on Sharp and Blunted Cones," AIAA Paper 2014-3108, 2014. doi:10.2514/6.2014-3108.

[11] Marineau, E., "Prediction Methodology for Second-Mode-Dominated Boundary-Layer Transition in Hypersonic Wind Tunnels," *AIAA Journal*, Vol. 55, No. 2, 2017, pp. 484–499. doi:10.2514/1.J055061.

[12] Jewell, J., and Kimmel, R., "Boundary Layer Stability Analysis for Stetson's Mach 6 Blunt Cone Experiments," *Journal of Spacecraft Rockets*, Vol. 54, No. 1, 2017, pp. 258–265. doi:10.2514/1.A33619.

[13] Jewell, J., Kennedy, R., Laurence, S., and Kimmel, R., "Transition on a Variable Bluntness 7-Degree Cone at High Reynolds Number," AIAA Paper 2018-1822, 2018. doi:10.2514/6.2018-1822.

[14] Dietz, G., and Hein, S., "Entropy-Layer Instabilities over a Blunted Flat Plate in Supersonic Flow," *Physics of Fluids*, Vol. 11, No. 1, 1999, pp. 7–9. doi:10.1063/1.869899.

[15] Fedorov, A., and Tumin, A., "Evolution of Disturbances in Entropy Layer on Blunted Plate in Supersonic Flow," *AIAA Journal*, Vol. 42, No. 1, 2004, pp. 89–94. doi:10.2514/1.9033.

[16] Choudhari, M., Li, F., and Edwards, J., "Stability Analysis of Roughness Array Wake in a High-Speed Boundary Layer," AIAA Paper 2009-0170, 2009. doi:10.2514/6.2009-170.

[17] Choudhari, M., Li, F., Chang, C., Norris, A., and Edwards, J., "Wake Instabilities Behind Discrete Roughness Elements in High Speed Boundary Layers," AIAA Paper 2013-0081, 2013. doi:10.2514/6.2013-81.

[18] Choudhari, M., Li, F., Chang, C., Edwards, J., Kegerise, M., and King, R., "Laminar-Turbulent Transition Behind Discrete Roughness Elements in a High-Speed Boundary Layer," AIAA Paper 2010-1575, 2013. doi:10.2514/6.2010-1575.

[19] Paredes, P., Choudhari, M., and Li, F., "Transition Delay via Vortex Generators in a Hypersonic Boundary Layer at Flight Conditions," AIAA Paper 2018-3217, 2018. doi:10.2514/6.2018-3217.

[20] Paredes, P., Choudhari, M., and Li, F., "Instability Wave-Streak Interactions in a Supersonic Boundary Layer," *Journal of Fluid Mechanics*, Vol. 831, 2017, pp. 524–553. doi:10.1017/jfm.2017.630.

[21] Chu, B.-T., "On the Energy Transfer to Small Disturbances in Fluid Flow (PART I)," *Acta Mechanica*, Vol. 1, No. 3, 1956, pp. 215–234. doi:10.1007/BF01387235.

[22] Mack, L. M., "Boundary Layer Stability Theory," Tech. Rep. Jet Propulsion Laboratory Report 900-277, California Institute of Technology, Pasadena, CA, 1969.

[23] Hanifi, A., Schmid, P., and Henningson, D., "Transient Growth in Compressible Boundary Layer Flow," *Physics of Fluids*, Vol. 8, 1996, pp. 826–837. doi:10.1063/1.868864.

[24] Theiss, A., Hein, S., Ali, S., and Radespiel, R., "Wake Flow Instability Studies Behind Discrete Roughness Elements on a Generic Re-Entry Capsule," AIAA Paper 2016-4382, 2016.

[25] Theiss, A., and Hein, S., "Investigation on the Wake Flow Instability Behind Isolated Roughness Elements on the Forebody of a Blunt Generic Reentry Capsule," *Progress in Flight Physics*, Vol. 9, 2017, pp. 451–480. doi:10.1051/eucass/201709451.

[26] Theiss, A., Leyh, S., and Hein, S., "Pressure Gradient Effects on Wake-Flow Instabilities Behind Isolated Roughness Elements on Re-Entry Capsules," *Proc. I. Mech. E. Part G: J Aerospace Engineering*, Vol. 234, No. 1, 2020, pp. 28–41. doi:10.1177/0954410019844067.

[27] Padilla-Montero, I., and Pinna, F., "Analysis of the Instabilities Induced by An Isolated Roughness Element in a Laminar High-Speed Boundary Layer," *Journal of Fluid Mechanics*, Vol. 915, 2021, p. A90. doi:10.1017/jfm.2021.70.

[28] De Tullio, N., Paredes, P., Sandham, N., and Theofilis, V., "Laminar-Turbulent Transition Induced by a Discrete Roughness Element in a Supersonic Boundary Layer," *Journal of Fluid Mechanics*, Vol. 735, 2013, pp. 613–646. doi:10.1017/jfm.2013.520.

[29] Choudhari, M., Li, F., and Paredes, P., "Effect of Distributed Patch of Smooth Roughness Elements on Transition in a High-Speed Boundary Layer," AIAA Paper 2018-3532, 2018. doi:10.2514/6.2018-3532.

[30] Di Giovanni, A., and Stemmer, C., "Cross-Flow-Type Breakdown Induced by Distributed Roughness in the Boundary Layer of a Hypersonic Capsule Configuration," *Journal of Fluid Mechanics*, Vol. 856, 2018, pp. 470–503. doi:10.1017/jfm.2018.706.

[31] Choudhari, M., Li, F., Paredes, P., and Duan, L., "Effect of 3D Roughness Patch on Instability Amplification in a Supersonic Boundary Layer," AIAA Paper 2019-0877, 2019. doi:10.2514/6.2019-0877.

[32] Garnaud, X., Lesshafft, L., Schmid, P., and Huerre, P., "The Preferred Mode of Incompressible Jets: Linear Frequency Response Analysis," *Journal of Fluid Mechanics*, Vol. 716, 2013, pp. 189–202. doi:10.1017/jfm.2012.540.

[33] Paredes, P., Choudhari, M., Li, F., and Chang, C.-L., "Optimal Growth in Hypersonic Boundary Layers," *AIAA Journal*, Vol. 54, No. 10, 2016, pp. 3050–3061. doi:10.2514/1.J054912.

[34] Hermanns, M., and Hernández, J., "Stable High-Order Finite-Difference Methods Based on Non-Uniform Grid Point Distributions," *International Journal for Numerical Methods in Fluids*, Vol. 56, 2008, pp. 233–255. doi:10.1002/fld.1510.

[35] Paredes, P., Hermanns, M., Le Clainche, S., and Theofilis, V., "Order 10^4 Speedup in Global Linear Instability Analysis using Matrix Formation," *Computer Methods in Applied Mechanics and Engineering*, Vol. 253, 2013, pp. 287–304. doi: 10.1016/j.cma.2012.09.014.

[36] Carpenter, M. H., Choudhari, M., L, F., Streett, C. L., and Chang, C.-L., "Excitation of Crossflow Instabilities in a Swept Wing Boundary Layer," AIAA Paper 2010-0378, 2010.

[37] Paredes, P., Choudhari, M., and Li, F., "Instability Wave-Streak Interactions in a High-Mach Number Boundary Layer at Flight Conditions," *Journal of Fluid Mechanics*, Vol. 858, 2018, pp. 474–499. doi:10.1017/jfm.2018.744.

[38] Litton, D., Edwards, J., and White, J., "Algorithmic Enhancements to the VULCAN Navier-Stokes Solver," AIAA Paper 2003-3979, 2003. doi:10.2514/6.2003-3979.

[39] Li, F., Choudhari, M., Paredes, P., and Duan, L., "High-Frequency Instabilities of Stationary Crossflow Vortices in a Hypersonic Boundary Layer," *Physical Review Fluids*, Vol. 1, 2016, pp. 053603–1–32. doi:10.1103/PhysRevFluids.1.053603.

[40] Wu, M., and Martin, M., "Direct Numerical Simulation of Supersonic Boundary Layer over a Compression Ramp," *AIAA Journal*, Vol. 45, No. 4, 2007, pp. 879–889. doi:10.2514/1.27021.

[41] Jiang, G., and Shu, C., "Efficient Implementation of Weighted ENO Schemes," *Journal of Computational Physics*, Vol. 126, No. 1, 1996, pp. 202–228. doi:10.1006/jcph.1996.0130.

[42] Williamson, J., "Low-Storage Runge-Kutta Schemes," *Journal of Computational Physics*, Vol. 35, No. 1, 1980, pp. 48–56. doi:10.1016/0021-9991(80)90033-9.

[43] Reda, D., and Leverance, R., "Boundary-Layer Transition Experiments on Pre-Ablated Graphite Nosetips in a Hyperballistics Range," NSWC-WOL-TR-76-71, Naval Surface Weapons Center, White Oak Laboratory, 1976.

[44] Reda, D., "Correlation of Nosetip Boundary-Layer Transition Data Measured in Ballistic Range Experiments," *AIAA Journal*, Vol. 19, No. 3, 1981, pp. 329–339. doi:10.2514/3.50952.

[45] Reda, D., "Review and Synthesis of Roughness-Dominated Transition Correlations for Reentry Applications," *Journal of Spacecraft Rockets*, Vol. 39, No. 2, 2002, pp. 161–167. doi:10.2514/2.3803.

[46] Reshotko, E., and Tumin, A., "Role of Transient Growth in Roughness-Induced Transition," *AIAA Journal*, Vol. 42, 2004, pp. 766–770. doi:10.2514/1.9558.

[47] Paredes, P., Choudhari, M., and Li, F., "Blunt-Body Paradox and Transient Growth on a Hypersonic Spherical Forebody," *Physical Review Fluids*, Vol. 2, 2017, p. 053903. doi:10.1103/PhysRevFluids.2.053903.

[48] Chou, A., Paredes, P., Kegerise, M., King, R., Choudhari, M., and Li, F., "Transition Induced by An Egg-Crate Roughness on a Flat Plate in Supersonic Flow," *Journal of Fluid Mechanics*, Vol. (submitted), 2022.